This is a non-peer reviewed preprint submitted to EarthArXiv; this manuscript is in review at Progress in Earth and Planetary Science.

Complex evolution of the 2016 Kaikoura earthquake revealed by teleseismic body waves

Kenta Ohara[1]

Email: kohrseismo@gmail.com

Yuji Yagi[2]

Corresponding author

Email: yagi-y@geol.tsukuba.ac.jp

Shinji Yamashita[1]

Email: ijnihsatihsamay@gmail.com

Ryo Okuwaki[2,3]

Email: rokuwaki@geol.tsukuba.ac.jp

Shiro Hirano[4]

Email: s-hrn@fc.ritsumei.ac.jp

This is a non-peer reviewed preprint submitted to EarthArXiv; this manuscript is in review at Progress in Earth and Planetary Science.

Yukitoshi Fukahata[5]

Email: fukahata@rcep.dpri.kyoto-u.ac.jp

(Institutional addresses)

[1] Graduate School of Science and Technology, University of Tsukuba, Tsukuba, Ibaraki 305-8572, Japan.

[2] Faculty of Life and Environmental Sciences, University of Tsukuba, Tsukuba, Ibaraki 305-8572, Japan.

[3] Mountain Science Center, University of Tsukuba, Tsukuba, Ibaraki 305-8572, Japan.

[4] College of Science and Engineering, Ritsumeikan University, Kusatsu, Shiga 525-8577, Japan

[5] Disaster Prevention Research Institute, Kyoto University, Uji, Kyoto 611-0011, Japan.

Abstract

The 2016 Kaikoura earthquake, New Zealand, ruptured more than a dozen faults, making it difficult to prescribe a model fault for analysing the event by inversion. To model this earthquake from teleseismic records, we used a potency density tensor inversion, which projects multiple fault slips onto a single model fault plane, reducing the non-uniqueness due to the uncertainty in selecting the faults' orientations. The resulting distribution of potency-rate density tensors is consistent with observed surface ruptures. In its initial stage, the rupture propagated northeastward primarily at shallow depths, and the rupture propagated northeastward at deep depths beneath a gap in reported surface ruptures. The main rupture phase started in the northeastern part of the Kekerengu fault after 50 s and propagated bilaterally to the northeast and southwest. The non-double-couple component grew to a large fraction of the source elements as the rupture went through the junction of the Jordan Thrust and the Papatea fault, which suggests that the rupture branched into both faults as it back-propagated toward the southwest. The potency density tensor inversion sheds new light on the irregular evolution of this earthquake, which produced a fault rupture pattern of unprecedented complexity. Our source model should provide new insights into source process of the 2016 Kaikoura earthquake (e.g., back-rupture propagation), which should prompt research to determine a more realistic model with segmented faults using near-field data.

Keywords

Earthquake dynamics, Waveform inversion, Body waves, Earthquake source observation

1 Introduction

On 13 November 2016, the Kaikoura earthquake struck in the South Island of New Zealand near the boundary between the Pacific and Australia plates (Fig. 1a). Field studies reported that the earthquake produced a complex set of surface ruptures of more than 12 faults (Hamling et al. 2017, Stirling et al. 2017, Litchfield et al. 2018). The rupture area, extending a total length of ∼165 km, can be divided into south and north sections separated by a gap of about 30 km with no mapped surface ruptures between the northeast end of the Conway-Charwell fault and the southwest end of the Manakau fault (Litchfield et al. 2018) (Fig. 1b). The south section involved the Humps fault and the Conway-Charwell fault with mixed dextral and reverse faulting (Litchfield et al. 2018) (Fig. 1b). The north section displayed a linear set of surface ruptures with mixed vertical and dextral displacements on the Manakau fault, the Upper Kowhai fault, the Jordan Thrust, the Kekerengu fault, and the Needles fault (Litchfield et al. 2018). In addition, surface rupture with mixed sinistral and reverse offsets occurred on the west-dipping Papatea fault, which extends southward nearly orthogonal to the linear rupture set near the junction of the Kekerengu fault and the Jordan Thrust (Litchfield et al. 2018) (Fig. 1b). Aftershocks were distributed throughout the zone of surface ruptures (Lanza et al. 2019) (Fig.

1b).

The Global Centroid Moment Tensor (GCMT) solution for the mainshock (Dziewonski et al. 1981, Ekström et al. 2012) indicates oblique reverse faulting (Fig. 1). A multiple-point-source inversion using the records of long-range seismographs (teleseismic waveforms) detects four subevents, consisting of three oblique strike-slip subevents and one thrust subevent (Duputel and Rivera 2017), indicating that the earthquake ruptured multiple faults with different faulting mechanisms. Finite-fault inversions using seismic data alone (Bai et al. 2017, Hollingsworth et al. 2017, Zhang et al. 2017, Zheng et al. 2018) or using both seismic and geodetic data (Cesca et al. 2017, Holden et al. 2017, Wang et al. 2018b) commonly find the initial rupture episode during the first ~60 s, followed by the main rupture episode, and discuss the rupture propagated toward northeast from the epicenter in both episodes. Notably, the field surveys identify large co-seismic deformation with sinistral and reverse offsets at the Papatea fault (Clark et al. 2017, Hamling et al. 2017, Stirling et al. 2017, Litchfield et al. 2018). However, finite-fault inversions using only teleseismic body waves, which can estimate the overall rupture propagation process during an earthquake, has not identified sub-events with focal mechanism corresponding to that Papatea fault rupture (Bai et al. 2017, Hollingsworth et al. 2017, Zhang et al. 2017).

Finite-fault inversions in previous studies estimated the rupture process under the assumption that the rupture unilaterally propagates northeastward (Bai et al. 2017, Cesca et al. 2017, Holden et al. 2017, Hollingsworth et al. 2017, Zhang et al. 2017, Wang et al. 2018b, Zheng et al. 2018). Such the strong constraints on the unilateral rupture scenario may not always be appropriate for the earthquake modeling in a complex fault zone, which sometimes involves the irregularity in rupture manner, including the back-rupture propagation as a part of its bilateral propagation that is initiated as a secondary rupture episode (e.g., Yamashita et al. 2022a, Yagi et al. 2023). The assumption of unilateral northeastward rupture propagation may make the interpretation of the inversion results more difficult. Indeed, it is difficult to explain how a right-lateral strike-slip rupture propagating in a northeast direction along the Jordan Thrust could have triggered a reverse fault rupture on the Papatea fault, situated in the extensional quadrant. Therefore, there should still be a room to investigate whether the source inversion only allowing for the unilateral rupture scenario should be a valid approach or not to adequately explain the rupture evolution along the unprecedentedly complex fault network.

As the 2016 Kaikoura earthquake includes multiple faults and complex fault geometries, finite-fault inversion assuming one or a few simplified model fault planes may produce erroneous inversion results due to modelling errors caused by the inappropriate assumed fault geometries (Shimizu et al. 2020). Thus, it is desirable to estimate the rupture process of the 2016 Kaikoura earthquake with a method, onto a model plane, like a potency density tensor inversion (PDTI) (Shimizu et al. 2020), instead of a method requiring assumption of fault geometries. The PDTI incorporates the uncertainty of the Green's function in the data covariance matrix (Yagi and Fukahata 2011) and introduces the Akaike's Bayesian Information Criterion (ABIC) (e.g., Akaike 1980, Yabuki and Matsu'ura 1992, Sato et al. 2022), making it possible to perform stable inversion analyses using seismic source model with a high degree of freedom in the rupture direction (e.g., Hicks et al. 2020, Yamashita et al. 2022a, Yagi et al. 2023).

In this study, we applied the PDTI to teleseismic P-waveforms of the 2016 Kaikoura earthquake to simultaneously estimate the rupture propagation and the focal mechanism variation. It revealed a source process consisting of an initial and a main rupture episode. The initial rupture propagates northeast from the hypocenter and breaks shallow and deep parts of the source area; deep rupture occurs where there is no surface rupture reported. Then the main rupture begins at the northeast end of the Kekerengu fault and propagates bilaterally to the northeast and southwest. An estimated fault geometry that incorporates variation in the focal mechanism is consistent with surface ruptures reported from the New Zealand Active Faults

Database (Langridge et al. 2016), and back-rupture propagation during the main rupture that branched out and propagated into the Jordan Thrust and the Papatea fault.

2 Methods, data, and modelling

The PDTI of teleseismic P-waveforms has been developed to mitigate the effect of the modelling error due to the inaccurate model fault geometries (Shimizu et al. 2020). Teleseismic P-waveforms are sensitive to perturbations in the focal mechanism but insensitive to errors in the source location, which is confirmed by both the synthetic tests and real applications (e.g., Shimizu et al., 2020; Tadapansawut et al., 2022; Yamashita et al., 2022b). Therefore, it should be critical to incorporate the focal mechanism change during the rupture propagation when building a seismic source model to robustly estimate the rupture process (Shimizu et al. 2020). In the PDTI, which is adopted in this study, fault slip along a model plane is described by a superposition of five basis double-couple components (Kikuchi and Kanamori 1991), then the rupture evolution (including perturbations in the focal mechanism) is estimated as a spatio-temporal distribution of the potency-rate density tensor (Ampuero and Dahlen 2005). Thus, the seismic waveform u_j observed at a station j is given by

$$u_j(t) = \sum_{q=1}^{5} \int_S \left(G_{qj}(t,\xi) + \delta G_{qj}(t,\xi)\right) * \dot{D}_q(t,\xi)\, d\xi + e_{bj}(t),$$

where G_{qj} is the Green's function of the qth basis double-couple moment tensor, δG_{qj} is the modelling error on G_{qj} (Yagi and Fukahata 2011), $\dot{D}_q$ is the potency-rate density function for the qth component of the basis double-couple moment tensor, e_{bj} is a background and instrumental Gausian noise, ξ represents a position on the assumed model plane (S), and $*$ denotes the convolution operator in the time domain.

Because this inversion allows any type of faulting mechanism on the assumed model plane, information about the fault geometry can be extracted from the observed data (Shimizu et al. 2020). To stably invert such a high degree-of-freedom seismic source model, the PDTI introduces the error term of the Green's function into the data covariance matrix (Yagi and Fukahata 2011), then evaluates the relative weights of information from observed data and prior constraints using Akaike's Bayesian Information Criterion (ABIC) (Akaike 1980, Yabuki and Matsu'ura 1992, Sato et al. 2022). This inversion formulation reduces the effect of modelling errors caused by uncertainties in fault geometry and Green's function and allows stable estimates of the seismic source process even when the predefined model plane deviates from the true fault plane (Shimizu et al. 2020). The PDTI has been effectively applied to earthquakes for which it is difficult to assume a reasonable fault model (Okuwaki et al. 2020, 2021, Tadapansawut et al. 2021, Yamashita et al. 2021, 2022a, Okuwaki and Fan 2022). This PDTI is thus suitable for analyzing the 2016 Kaikoura earthquake, with its complex distribution of surface ruptures, in enabling us to project multiple fault ruptures onto a single assumed model plane (Okuwaki et al. 2021, Yamashita et al. 2022a).

For the PDTI, we used the teleseismic P-waveforms (vertical component) from 48 stations at epicentral distances of 30°–100° downloaded from the Data Management Center of the Incorporated Research Institutions for Seismology (IRIS-DMC) (Fig. 2a). We converted the waveform data to velocity waveforms at a sampling interval of 0.8 s. We calculated Green's functions at a sampling interval of 0.1 s by the method of Kikuchi and Kanamori (Kikuchi and Kanamori 1991). We used CRUST2.0 (Bassin et al. 2000) as a 1-D structure model around the source (see Supplementary Table S1), and set the value of t*, which controls the inelastic attenuation of P-waves, to 1 s. We aligned the P-wave first motion manually to correct the travel-time deviations due to 3-D earth structure (e.g., Fan and Shearer, 2015). The effect of uncertainty of underground structure was mitigated by introducing the error term of the Green's function into the data covariance matrix (Yagi and Fukahata 2011).

Because the high-frequency component of the teleseismic body waveforms is effectively suppressed owing to the natural low-pass filtering caused by inelastic attenuation, given a sufficiently short resampling interval, the waveforms are little affected by aliasing (see

Supplementary Fig. S1). Conversely, applying a low-pass filter that includes an anti-aliasing filter increases the off-diagonal component of the data covariance matrix (Yagi and Fukahata 2011), making it difficult to stably invert the data covariance matrix. We exploited this natural filtering to obtain a more stable analysis by not using a low-pass filter on the waveforms or Green's functions. As a result, we were able to estimate a solution that reproduced the features of the observed waveform without distortion by low-pass filtering (Fig. 2b, Supplementary Fig. S2).

We adopted a hypocenter location at 172.95°E, 42.62°S, and 15 km depth (Lanza et al. 2019). We established a 200 km × 35 km vertical model plane striking NE–SW (230°) to represent surface ruptures (Langridge et al. 2016, Hamling et al. 2017, Stirling et al. 2017, Litchfield et al. 2018) and aftershock activity (Lanza et al. 2019) (Fig. 1b). We set a maximum rupture velocity of 2.6 km/s to allow for the northeastward migration of the high-frequency source at about 2.0 km/s indicated by P-waveform back-projection (Xu et al. 2018). The slip on the model plane was expanded by linear B-spline functions in space with an interval of 10 km and 5 km in the strike and dip directions, respectively, and by linear B-spline functions in time with an interval of 0.8 s with a maximum duration of 60 s for each source element, which is long enough to detect possible re-rupture and/or back rupture propagation (Holden et al. 2017, Hicks et al. 2020). The total duration of the event was set to 95 s. The ABIC can prevent overfitting, even using large number of model parameters (Sato et al. 2022).

We applied a time-adaptive smoothing constraint that adjusts the smoothing strength in inverse proportion to the changing amplitude of the potency-rate function (Yamashita et al. 2022b). This constraint can mitigate the problem of oversmoothing during the main rupture, which obscures the results (Yamashita et al. 2022b).

3 Results

We estimated the distribution of potency-rate density tensors on the assumed vertical model plane, then time-integrated them at each source element to yield the spatial distribution of potency density tensors shown in Fig. 2c. This figure shows an area of high potency density centered around 110 km northeast of the epicenter on the shallow part of the model plane. The dominant focal mechanism (with relatively large potency density) differs along the length of the fault plane, being oblique reverse slip for 50–120 km and strike-slip for 130–150 km northeast of the epicenter (Fig. 2c). The total seismic moment is 1.1×10^{21} Nm. The moment-rate function, obtained by calculating the seismic moment-rate of the best-fitted double-couple source at each sampling time, shows that the moment rate is around 1.0×10^{19} Nm/s until 55 s from the origin time and then increases rapidly, reaching 6.0×10^{19} Nm/s at 66 s (Fig. 2d).

Figure 3 shows selected snapshots of the potency-rate density tensors on a cross section of the model fault plane; see Supplementary Figure S3 for the full set of snapshots. Figure 4 is a map view of the strike angles of the nodal planes of these tensors along the top of the model plane. During the first 10 s from the origin time, a strike-slip rupture striking about 25° clockwise from the model plane propagated to the northeast of the epicenter (Figs. 3a, 4). Hereafter, we refer to the origin time as 0s. The rupture then propagated further northeastward on the shallow part of the model plane, changing to an oblique reverse focal mechanism. This shallow rupture stagnated at about 40 km northeast of the epicenter after 20 s; however, a deeper rupture continued on the model plane during 20–30 s, reaching 70 km northeast of the epicenter. An isolated reverse rupture occurred at 25–30 s near the ground surface around the epicenter. During 30–45 s, an oblique reverse rupture appeared near the ground surface about 70 km northeast of the epicenter and propagated northeast; during 45–50 s, the rupture propagation pattern was obscure (see Supplementary Fig. S3a).

After 50 s, the main rupture emerged near the ground surface about 110 km northeast of the epicenter and propagated bilaterally to the northeast and southwest (Figs. 3, S4). During 50–55 s, the dominant focal mechanisms were mixed reverse and strike-slip with the right-lateral nodal plane oriented about 40° clockwise from the model plane (Figs. 3a, 4). The northeastward rupture, a strike-slip rupture striking about 10° counterclockwise from the model plane, propagated through the shallow part of the model plane and reached the edge of the model plane at about 68 s (Figs. 3b, 4). The southwestward rupture reached about 70 km northeast of the epicenter by 70 s (Fig. 3b). During 60–64 s, it was dominantly strike-slip near the ground surface and reverse in the deep part of the model plane (Fig. 3b). The reverse slip component increased with time after 64 s. The rupture gradually weakened after 70 s and ceased at 95 s. The inverted solution well explains the teleseismic P-waveforms (Fig. 2b, Supplementary Fig. S2).

4 Reproducibility and sensitivity tests

We performed a numerical experiment to test the stability and reproducibility of our potency-rate density tensor distribution. Using the obtained source model as an input model, we generated synthetic waveforms for the 48 stations used in the analysis by convoluting the obtained solution with the Green's function used in the analysis for real waveforms plus an error for the Green's function, and then adding background noise (Shimizu et al. 2020) (see Supplementary Fig. S5). The resulting synthetic waveforms were inverted with the same settings used with the real waveforms.

We performed a structure sensitivity test using the 1-D structure model CRUST1.0 (Laske et al. 2013) for the source region instead of CRUST2.0 (Bassin et al. 2000) (see Supplementary Table S2). We estimated the rupture evolution using the same observed dataset and the same inversion settings as for our preferred modelling.

We also performed another sensitivity test projecting rupture process onto the horizontal model plane. We established a 200 km × 70 km horizontal model plane striking NE–SW (230°) to represent surface ruptures (Langridge et al. 2016, Hamling et al. 2017, Stirling et al. 2017, Litchfield et al. 2018) and aftershock activity (Lanza et al. 2019) (see Supplementary Fig. S8). The slip on the model plane was expanded by bilinear B-spline functions in space with an interval of 10 km. The hypocentral depth was 10 km, where rupture mainly detected in the analysis using vertical model plane (Figs. 2 and 3). We used the same observed dataset and the same inversion settings as for our preferred modelling using the vertical plane.

Both the reproducibility and structure sensitivity tests successfully reproduced the features in our preferred model: these included the initial strike-slip rupture during the first 10 s, the northeast-propagating oblique reverse rupture at varying depths during 10–30 s and re-appearing near the ground surface about 70 km northeast of the epicenter, and the main bilateral rupture starting about 110 km northeast of the epicenter around 50 s with a strike-slip rupture propagating northeast and an oblique-slip rupture propagating southwest (see Supplementary Figs. S6, S7). Although the sensitivity test using the horizontal model plane does not have depth resolution, the aforementioned lateral variation of rupture evolution was also detected (see Supplementary Fig. S8).

5 Discussion

Our result shows that the rupture process of the 2016 Kaikoura earthquake can be divided into initial and main rupture episodes: the initial rupture propagated northeastward; the main rupture propagated bilaterally from 110 km northeast of the epicenter, involving backward rupture propagation toward the epicenter. The total moment tensor shows oblique reverse faulting, which is consistent with the GCMT solution (Fig. 1). In the following, we will discuss how those rupture episodes relate to the observed surface ruptures, to unravel the unprecedentedly complex rupture process of the 2016 Kaikoura earthquake.

As the initial strike-slip rupture propagated northeast during the first 10 s (Fig. 3a), the right-lateral nodal planes of the potency-rate density tensors matched the strike of the Humps fault (Langridge et al. 2016) (Fig. 4). An oblique reverse rupture then propagated northeast through the shallow part of the model plane. After 20 s, the shallow rupture stagnated about 40 km northeast of the epicenter while the oblique reverse rupture continued to propagate deeper on the model plane (Fig. 3a). The location where the shallow rupture stagnated corresponds to the gap in surface ruptures between the Conway-Charwell and Manakau faults (Langridge et al. 2016) (Figs. 1, 3a), and the deep oblique reverse slip has also been identified by the finite-fault inversion of geodetic data (Hamling et al. 2017). During 30–35 s, oblique reverse rupture appeared near the ground surface about 70 km northeast of the epicenter, corresponding to the southwest end of the Manakau fault (Langridge et al. 2016), and then propagated near the ground surface until 45 s (Fig. 3a). Our results show that the initial rupture shifted deeper around the area of no surface rupture during 20–30 s. However, because slips on multiple fault planes are projected onto the single model plane in our inversion, it is difficult to determine whether these ruptures were connected at depth. It is controversial how the plate interface contributed to moment release in the 2016 Kaikoura earthquake (e.g., Lanza et al., 2019). Although the deep rupture during 20–30 s appeared at about 25 km depth, the resolved dip angles (~40°) are steeper than those of the hypothesised plate interface (e.g., Williams et al., 2013).

After 50 s, the main rupture appeared in the northeast part of the Kekerengu fault (Langridge et al. 2016) and then propagated bilaterally until about 70 s, such that one end of the rupture appeared to propagate backward toward the epicenter (Fig. 3). Because we cannot trace the rupture migration during 45–50 s, it is difficult to determine how the initial rupture migrated to the main rupture. The potency-rate density tensors obtained at 50–55 s indicate both strike-slip and reverse faulting, and the strikes of their right-lateral nodal planes are consistent with that of the northeastern Kekerengu fault (Langridge et al. 2016) (Fig. 4). For the northeastward strike-slip rupture, the strikes of the right-lateral nodal planes match the orientation of the Needles fault (Langridge et al. 2016) (Fig. 4), and the dominance of strike-slip faulting in the shallow part of the model plane (Fig. 3b) is consistent with other studies (Bai et al. 2017, Cesca et al. 2017, Hollingsworth et al. 2017, Wang et al. 2018a, 2018b, Zheng et al. 2018, Xu et al. 2018, Mouslopoulou et al. 2019). For the backward rupture, the potency-rate density tensors near the ground surface show a transition from oblique strike-slip to oblique reverse faulting 80–110 km northeast of the epicenter (Fig. 3b), and the strikes of the right-lateral or northwest-dipping nodal planes match those of the central Kekerengu fault and the Jordan Thrust (Langridge et al. 2016) (Fig. 4).

The potency-rate density tensors around the Jordan Thrust and Papatea fault contain large non-double-couple components, reaching an 80% maximum from 60 to 66 s, that then rapidly decrease to less than 20% after 66 s (Fig. 5). Our reproducibility tests also captured the time variation of this component (see Supplementary Figs. S6, S7). The size of the non-double-couple component from 60 to 66 s suggests that slips occurred on multiple faults with different orientations; this is consistent with reverse faulting with sinistral strike-slip reported on the Papatea fault (Hamling et al. 2017, Stirling et al. 2017, Litchfield et al. 2018, Wang et al. 2018b, Xu et al. 2018), which is nearly perpendicular to the other surface ruptures (see Supplementary Fig. S9). Our result suggests that the backward rupture on the Kekerengu fault not only propagated into the Jordan Thrust, but also branched out and propagated into the Papatea fault. Given the right-lateral strike-slip rupture propagates in a southwest direction along the Kekerengu fault, the Papatea fault is situated in the compressional quadrant; this suggests that the southwestward rupture along the Kekerengu fault can better explain a trigger of the reverse faulting rupture along the Papatea fault than the northeastward rupture along the Jordan Thrust, which should require the Papatea fault to be located in the extensional quadrant. Although we find it reasonable to explain the Papatea rupture by our series of bilateral ruptures, more detailed analyses and simulations incorporating the detailed geometries of those faults will be required to testify which of the scenarios is more favorable for the Papatea rupture. Near the southwest end of that rupture, the strikes of the right-lateral or northwest-dipping nodal planes were about 10° clockwise from the model plane, which is consistent with the strikes of the Upper Kowhai and Manakau faults (Langridge et al. 2016) (Fig. 4). So far, an earthquake source modelling has often been relying on a restricted degree of freedom, which has been considered as a requirement for a plausible solution. However, the modelling employing fewer degrees of freedom might be easy to drop information that are recorded in the observed data and critical to interpret the source process (e.g., Shimizu et al., 2020), albeit the solution derived from those modelling apparently looks not bad. One of the advantages of employing a model with a high degree of freedom (e.g., this study) is that a solution is less susceptible to the modellers' preconceptions. By estimating the potency tensor density distribution including the non-double-couple component, we found that the backward rupture branched out and propagated on the Papatea fault, which, to our best knowledge, has not been reported in previous attempts of the teleseismic body waves analyses.

Our analysis suggests the following scenario for the main rupture: it propagated bilaterally from the northeast part of the Kekerengu fault, the northeastward rupture propagating along the Needles fault and the southwestward rupture propagating along the Kekerengu fault, Jordan Thrust, Papatea, Upper Kowhai, and Manakau faults. We interpret the simultaneous rupture events in the area around the Needles fault and the Jordan Thrust noted in previous studies (Bai et al. 2017, Cesca et al. 2017, Hollingsworth et al. 2017) as bilateral rupture propagation. In addition, the back-projection image (Xu et al. 2018) shows that the seismic wave radiation point moves toward the epicenter from around the south edge of the Papatea fault during 50–70 s, a finding consistent with backward rupture propagation.

In the region of the backward rupture, multiple faults may have ruptured during the initial rupture phase, because the aftershock region extends perpendicular to the model plane and the focal mechanisms varied during the initial rupture (Fig. 6). Because our model fault plane may include projections of multiple independent ruptures, we cannot determine which faults participated in the initial rupture. Therefore, we cannot say whether the backward rupture was a re-rupture (Holden et al. 2017) or a rupture on a different fault, as in the 2010 El Mayor–Cucapah earthquake (Yamashita et al. 2022a).

Back-propagating ruptures in seismic events are not so rare; they have been reported in the 2010 El Mayor–Cucapah earthquake (Yamashita et al. 2022a), the 2011 Tohoku-oki earthquake (Ide et al. 2011), the 2014 Iquique earthquake (Yagi et al. 2014), the 2016 Romanche transform-fault earthquake (Hicks et al. 2020), and the 2018 Peru earthquake (Hu et al. 2021). With the exception of the 2011 Tohoku-oki earthquake, where the backward rupture followed an overshooting rupture near the free surface (Ide et al. 2011), these earthquakes have in common an initial weak rupture which triggers a main rupture, at a point distant from the hypocenter, that involves a back-propagating rupture. It appears that the 2016 Kaikoura earthquake is another example of this kind of event.

Our modelling approach requires few assumptions of modelling, that is, we solve for multiplicity of fault configuration and diverse rupture geometries on the flat single model fault. This is still prone to non-uniqueness in the Kaikoura rupture, primarily due to the limited spatial resolution of tele-seismic records, but the rupture directions and timing, involving back-rupture propagation resolved in our model, in turn, can be useful for further inverse and/or forward modelling using near-field datasets, which contribute to converge to a realistic source model of the Kaikoura earthquake.

6 Conclusions

We obtained the source process of the 2016 Kaikoura earthquake by a potency density tensor inversion from teleseismic P-waveform data, a method for which we did not need to strictly define the fault geometry and rupture directions. We found a complex episode including an initial unilateral and a delayed main bilateral rupture, and the variations of the focal mechanisms are consistent with the reported surface ruptures. The initial rupture propagated northeastward at deep depths, when it passed through a gap in reported surface ruptures. The main rupture involved the southwestward back-rupture propagation, and it branched out and propagated into the Jordan Thrust and Papatea fault from the Kekerengu fault. Our result suggests that tele-seismic waveform data can resolve such a complex rupture process (e.g., the bilateral rupture, including rupture bifurcation to the Papatea fault), and the potency density tensor inversion approach of projecting slips on multiple faults onto a single model plane, as opposed to an approach of prescribing fault planes, is useful for analyzing earthquakes with complex fault geometries.

Abbreviations

GCMT: Global Centroid Moment Tensor; PDTI: Potency density tensor inversion

Declarations

Availability of data and material

All seismic data were downloaded through the IRIS Wilber 3 system (https://ds.iris.edu/wilber3/) or IRIS Web Services (https://service.iris.edu/), including the following seismic networks: (1) BDSN (https://doi.org/10.7932/BDSN), (2) SCSN (https://doi.org/10.7914/SN/CI), (3) GEOSCOPE (https://doi.org/10.18715/GEOSCOPE.G), (4) GEOFON (https://doi.org/10.14470/TR560404), (5) the Global Telemetered Seismograph

Network (https://doi.org/10.7914/SN/GT), (6) the Hong Kong Seismograph Network, (7) the New China Digital Seismograph Network (https://doi.org/10.7914/SN/IC), (8) the IRIS/IDA Seismic Network (https://doi.org/10.7914/SN/II), and (9) the Global Seismograph Network (https://doi.org/10.7914/SN/IU). The CRUST1.0 and CRUST2.0 structural velocity models are available from https://igppweb.ucsd.edu/~gabi/crust1.html and https://igppweb.ucsd.edu/~gabi/crust2.html, respectively.

Competing interests

The authors declare no competing interests. Correspondence and requests for materials should be addressed to K.O. or Y.Y.

Funding

This work was supported by Grant-in-Aid for Scientific Research (C) 22K03751 from the Ministry of Education, Culture, Sports, Science and Technology (MEXT).

Authors' contributions

K.O. and Y.Y. designed this study, compiled the data, and performed the analyses. All authors interpreted the research results. K.O. prepared figures and wrote the manuscript, which was revised by Y.Y., S.Y., R.O., S.H., and Y.F. All authors approved the manuscript. All authors agreed both to be personally accountable for their own contributions and to ensure that questions related to the accuracy or integrity of any part of the work were appropriately investigated and resolved and their resolution documented in the literature.

Acknowledgements

We thank Federica Lanza for providing her relocated aftershock data (Lanza et al. 2019). The facilities of IRIS Data Services, and specifically the IRIS Data Management Center, provided access to waveforms, related metadata, and derived products used in this study. IRIS Data Services are funded through the Seismological Facilities for the Advancement of Geoscience (SAGE) Award of the National Science Foundation under Cooperative Support Agreement EAR-1851048. We used FPSPACK (Gasperini and Vannucii 2003) software to handle the focal mechanism obtained in the inversion. The code for the PDTI was developed by Yuji Yagi, Kosuke Shimizu, and Shinji Yamashita. All of the figures were generated with matplotlib (v3.4.0:https://doi.org/10.1109/MCSE.2007.55) (Hunter 2007) and Pyrocko (v2021.9.14:https://doi.org/10.5880/GFZ.2.1.2017.001) (Heimann et al. 2017).

References

Akaike, H. 1980. Likelihood and the Bayes procedure. Trabajos de Estadistica Y de Investigacion Operativa, **31**: 143–166. doi:10.1007/BF02888350.

Ampuero, J.-P., and Dahlen, F.A. 2005. Ambiguity of the Moment Tensor. Bulletin of the Seismological Society of America, **95**: 390–400. doi:10.1785/0120040103.

Bai, Y., Lay, T., Cheung, K.F., and Ye, L. 2017. Two regions of seafloor deformation generated the tsunami for the 13 November 2016, Kaikoura, New Zealand earthquake. Geophysical Research Letters, **44**: 6597–6606. doi:10.1002/2017GL073717.

Bassin, C., Laske, G., and Masters, G. 2000. The Current Limits of Resolution for Surface Wave Tomography in North America. EOS Trans AGU, **81**.

Bird, P. 2003. An updated digital model of plate boundaries. Geochemistry, Geophysics, Geosystems, **4**. doi:10.1029/2001GC000252.

Cesca, S., Zhang, Y., Mouslopoulou, V., Wang, R., Saul, J., Savage, M., Heimann, S., Kufner, S.K., Oncken, O., and Dahm, T. 2017. Complex rupture process of the Mw 7.8, 2016, Kaikoura earthquake, New Zealand, and its aftershock sequence. Earth and Planetary Science Letters, **478**: 110–120. Elsevier B.V. doi:10.1016/j.epsl.2017.08.024.

Clark, K.J., Nissen, E.K., Howarth, J.D., Hamling, I.J., Mountjoy, J.J., Ries, W.F., Jones, K., Goldstien, S., Cochran, U.A., Villamor, P., Hreinsdóttir, S., Litchfield, N.J., Mueller, C., Berryman, K.R., and Strong, D.T. 2017. Highly variable coastal deformation in the 2016 MW7.8 Kaikōura earthquake reflects rupture complexity along a transpressional plate boundary. Earth and Planetary Science Letters, **474**: 334–344. Elsevier B.V. doi:10.1016/j.epsl.2017.06.048.

DeMets, C., Gordon, R.G., Argus, D.F., and Stein, S. 1994. Effect of recent revisions to the geomagnetic reversal time scale on estimates of current plate motions. Geophysical Research Letters, **21**: 2191–2194. doi:10.1029/94GL02118.

Duputel, Z., and Rivera, L. 2017. Long-period analysis of the 2016 Kaikoura earthquake. Physics of the Earth and Planetary Interiors, **265**: 62–66. doi:10.1016/j.pepi.2017.02.004.

Dziewonski, A.M., Chou, T.A., and Woodhouse, J.H. 1981. Determination of earthquake source parameters from waveform data for studies of global and regional seismicity. Journal of Geophysical Research, **86**: 2825–2852. doi:10.1029/JB086iB04p02825.

Ekström, G., Nettles, M., and Dziewoński, A.M. 2012. The global CMT project 2004–2010: Centroid-moment tensors for 13,017 earthquakes. Physics of the Earth and Planetary Interiors, **200–201**: 1–9. Elsevier. doi:10.1016/j.pepi.2012.04.002.

Fan, W., and Shearer, P.M. 2015. Detailed rupture imaging of the 25 April 2015 Nepal earthquake using teleseismic P waves. Geophysical Research Letters, **42**: 5744–5752.

doi:10.1002/2015GL064587.

Frohlich, C. 2001. Display and quantitative assessment of distributions of earthquake focal mechanisms. Geophysical Journal International, **144**: 300–308. doi:10.1046/j.1365-246x.2001.00341.x.

Gasperini, P., and Vannucii, G. 2003. FPSPACK: a package of FORTRAN subroutines to manage earthquake focal mechanism data. Computers & Geosciences, **29**: 893–901. doi:10.1016/S0098-3004(03)00096-7.

Hamling, I.J., Hreinsdóttir, S., Clark, K., Elliott, J., Liang, C., Fielding, E., Litchfield, N., Villamor, P., Wallace, L., Wright, T.J., D'Anastasio, E., Bannister, S., Burbidge, D., Denys, P., Gentle, P., Howarth, J., Mueller, C., Palmer, N., Pearson, C., Power, W., Barnes, P., Barrell, D.J.A., van Dissen, R., Langridge, R., Little, T., Nicol, A., Pettinga, J., Rowland, J., and Stirling, M. 2017. Complex multifault rupture during the 2016 Mw 7.8 Kaikōura earthquake, New Zealand. Science, **356**. doi:10.1126/science.aam7194.

Heimann, S., Kriegerowski, M., Isken, M., Cesca, S., Daout, S., Grigoli, F., Juretzek, C., Megies, T., Nooshiri, N., Steinberg, A., Sudhaus, H., Vasyura-Bathke, H., Willey, T., and Dahm, T. 2017. Pyrocko - An open-source seismology toolbox and library. GFZ Data Services. doi:10.5880/GFZ.2.1.2017.001.

Hicks, S.P., Okuwaki, R., Steinberg, A., Rychert, C.A., Harmon, N., Abercrombie, R.E., Bogiatzis, P., Schlaphorst, D., Zahradnik, J., Kendall, J.M., Yagi, Y., Shimizu, K., and Sudhaus, H. 2020. Back-propagating supershear rupture in the 2016 M w 7.1 Romanche transform fault earthquake. Nature Geoscience, **13**: 647–653. doi:10.1038/s41561-020-0619-9.

Holden, C., Kaneko, Y., D'Anastasio, E., Benites, R., Fry, B., and Hamling, I.J. 2017. The 2016 Kaikōura Earthquake Revealed by Kinematic Source Inversion and Seismic Wavefield Simulations: Slow Rupture Propagation on a Geometrically Complex Crustal Fault Network. Geophysical Research Letters, **44**: 11,320-11,328. doi:10.1002/2017GL075301.

Hollingsworth, J., Ye, L., and Avouac, J.P. 2017. Dynamically triggered slip on a splay fault in the Mw 7.8, 2016 Kaikoura (New Zealand) earthquake. Geophysical Research Letters, **44**: 3517–3525. doi:10.1002/2016GL072228.

Hu, Y., Yagi, Y., Okuwaki, R., and Shimizu, K. 2021. Back-propagating rupture evolution within a curved slab during the 2019 Mw8.0 Peru intraslab earthquake. Geophysical Journal International, **227**: 1602–1611. Oxford University Press. doi:10.1093/gji/ggab303.

Hunter, J.D. 2007. Matplotlib: A 2D graphics environment. Computer Science and Engineering, **9**: 90–95. doi:10.1109/MCSE.2007.55.

Ide, S., Baltay, A., and Beroza, G.C. 2011. Shallow dynamic overshoot and energetic deep rupture in the 2011 M w 9.0 Tohoku-Oki earthquake. Science, **332**: 1426–1429.

doi:10.1126/SCIENCE.1207020/SUPPL_FILE/1207020-IDE-SOM.PDF.

Kikuchi, M., and Kanamori, H. 1991. Inversion of complex body waves—III. Bulletin of the Seismological Society of America, **81**: 2335–2350. doi:10.1785/BSSA0810062335.

Langridge, R., Ries, W., Litchfield, N., Villamor, P., van Dissen, R., Barrell, D., Rattenbury, M., Heron, D., Haubrock, S., Townsend, D., Lee, J., Berryman, K., Nicol, A., Cox, S., and Stirling, M. 2016. The New Zealand Active Faults Database. New Zealand Journal of Geology and Geophysics, **59**: 86–96. doi:10.1080/00288306.2015.1112818.

Lanza, F., Chamberlain, C.J., Jacobs, K., Warren-Smith, E., Godfrey, H.J., Kortink, M., Thurber, C.H., Savage, M.K., Townend, J., Roecker, S., and Eberhart-Phillips, D. 2019. Crustal Fault Connectivity of the M $_w$ 7.8 2016 Kaikōura Earthquake Constrained by Aftershock Relocations. Geophysical Research Letters, **46**: 6487–6496. Blackwell Publishing Ltd. doi:10.1029/2019GL082780.

Laske, G., Masters, G., Ma, Z., and Pasyanos, M. 2013. Update on CRUST1.0 - A 1-degree Global Model of Earth's Crust. Geophysical Research Abstracts, **15**.

Litchfield, N.J., Villamor, P., van Dissen, R.J., Nicol, A., Barnes, P.M., Barrell, D.J.A., Pettinga, J.R., Langridge, R.M., Little, T.A., Mountjoy, J.J., Ries, W.F., Rowland, J., Fenton, C., Stirling, M.W., Kearse, J., Berryman, K.R., Cochran, U.A., Clark, K.J., Hemphill-Haley, M., Khajavi, N., Jones, K.E., Archibald, G., Upton, P., Asher, C., Benson, A., Cox, S.C., Gasston, C., Hale, D., Hall, B., Hatem, A.E., Heron, D.W., Howarth, J., Kane, T.J., Lamarche, G., Lawson, S., Lukovic, B., McColl, S.T., Madugo, C., Manousakis, J., Noble, D., Pedley, K., Sauer, K., Stahl, T., Strong, D.T., Townsend, D.B., Toy, V., Williams, J., Woelz, S., and Zinke, R. 2018. Surface rupture of multiple crustal faults in the 2016 Mw 7.8 Kaikōura, New Zealand, earthquake. Bulletin of the Seismological Society of America, **108**: 1496–1520. doi:10.1785/0120170300.

Mitchell, J.S., Mackay, K.A., Neil, H.L., Mackay, E.J., Pallentin, A., and Notman, P. 2012. Undersea New Zealand, 1:5,000,000. NIWA Chart, Miscellaneous Series, **92**.

Mouslopoulou, V., Saltogianni, V., Nicol, A., Oncken, O., Begg, J., Babeyko, A., Cesca, S., and Moreno, M. 2019. Breaking a subduction-termination from top to bottom: The large 2016 Kaikōura Earthquake, New Zealand. Earth and Planetary Science Letters, **506**: 221–230. Elsevier B.V. doi:10.1016/j.epsl.2018.10.020.

Okuwaki, R., and Fan, W. 2022, January 28. Oblique Convergence Causes Both Thrust and Strike-Slip Ruptures During the 2021 M 7.2 Haiti Earthquake. John Wiley and Sons Inc. doi:10.1029/2021GL096373.

Okuwaki, R., Hicks, S.P., Craig, T.J., Fan, W., Goes, S., Wright, T.J., and Yagi, Y. 2021, December 28. Illuminating a Contorted Slab With a Complex Intraslab Rupture Evolution During the 2021 Mw 7.3 East Cape, New Zealand Earthquake. John Wiley and Sons Inc.

doi:10.1029/2021GL095117.

Okuwaki, R., Hirano, S., Yagi, Y., and Shimizu, K. 2020. Inchworm-like source evolution through a geometrically complex fault fueled persistent supershear rupture during the 2018 Palu Indonesia earthquake. Earth and Planetary Science Letters, **547**. Elsevier B.V. doi:10.1016/j.epsl.2020.116449.

Sato, D.S.K., Fukahata, Y., and Nozue, Y. 2022. Appropriate reduction of the posterior distribution in fully Bayesian inversions. Geophysical Journal International,. Oxford University Press (OUP). doi:10.1093/gji/ggac231.

Shimizu, K., Yagi, Y., Okuwaki, R., and Fukahata, Y. 2020. Development of an inversion method to extract information on fault geometry from teleseismic data. Geophysical Journal International, **220**: 1055–1065. Oxford University Press. doi:10.1093/gji/ggz496.

Stirling, M.W., Litchfield, N.J., Villamor, P., van Dissen, R.J., Nicol, A., Pettinga, J., Barnes, P., Langridge, R.M., Little, T., Barrell, D.J.A., Mountjoy, J., Ries, W.F., Rowland, J., Fenton, C., Hamling, I., Asher, C., Barrier, A., Benson, A., Bischoff, A., Borella, J., Carne, R., Cochran, U.A., Cockroft, M., Cox, S.C., Duke, G., Fenton, F., Gasston, C., Grimshaw, C., Hale, D., Hall, B., Hao, K.X., Hatem, A., Hemphill-Haley, M., Heron, D.W., Howarth, J., Juniper, Z., Kane, T., Kearse, J., Khajavi, N., Lamarche, G., Lawson, S., Lukovic, B., Madugo, C., Manousakis, I., Mccoll, S., Noble, D., Pedley, K., Sauer, K., Stah, T., Strong, D.T., Townsend, D.B., Toy, V., Villeneuve, M., Wandres, A., Williams, J., Woelz, S., and Zinke, R. 2017. THE M W 7.8 2016 KAIKŌURA EARTHQUAKE: SURFACE FAULT RUPTURE AND SEISMIC HAZARD CONTEXT. Bulletin of the New Zealand Society for Earthquake Engineering, **50**: 73–84. [accessed 3 March 2022].

Tadapansawut, T., Okuwaki, R., Yagi, Y., and Yamashita, S. 2021. Rupture Process of the 2020 Caribbean Earthquake Along the Oriente Transform Fault, Involving Supershear Rupture and Geometric Complexity of Fault. Geophysical Research Letters, **48**. doi:10.1029/2020GL090899.

Tadapansawut, T., Yagi, Y., Okuwaki, R., Yamashita, S., and Shimizu, K. 2022. Complex rupture process on the conjugate fault system of the 2014 Mw 6.2 Thailand earthquake. Progress in Earth and Planetary Science, **9**. Springer Science and Business Media Deutschland GmbH. doi:10.1186/s40645-022-00484-5.

Wang, D., Chen, Y., Wang, Q., and Mori, J. 2018a. Complex rupture of the 13 November 2016 Mw 7.8 Kaikoura, New Zealand earthquake: Comparison of high-frequency and low-frequency observations. Tectonophysics, **733**: 100–107. Elsevier. doi:10.1016/j.tecto.2018.02.004.

Wang, T., Wei, S., Shi, X., Qiu, Q., Li, L., Peng, D., Weldon, R.J., and Barbot, S. 2018b. The 2016 Kaikōura earthquake: Simultaneous rupture of the subduction interface and overlying faults. Earth and Planetary Science Letters, **482**: 44–51. Elsevier B.V. doi:10.1016/j.epsl.2017.10.056.

Williams, C.A., Eberhart-Phillips, D., Bannister, S., Barker, D.H.N., Henrys, S., Reyners, M., and Sutherland, R. 2013. Revised Interface Geometry for the Hikurangi Subduction Zone, New Zealand. Seismological Research Letters, **84**: 1066–1073. doi:10.1785/0220130035.

Xu, W., Feng, G., Meng, L., Zhang, A., Ampuero, J.P., Bürgmann, R., and Fang, L. 2018. Transpressional Rupture Cascade of the 2016 M_w 7.8 Kaikoura Earthquake, New Zealand. Journal of Geophysical Research: Solid Earth, **123**: 2396–2409. doi:10.1002/2017JB015168.

Yabuki, T., and Matsu'ura, M. 1992. Geodetic data inversion using a Bayesian information criterion for spatial distribution of fault slip. Geophysical Journal International, **109**: 363–375. doi:10.1111/j.1365-246X.1992.tb00102.x.

Yagi, Y., and Fukahata, Y. 2011. Introduction of uncertainty of Green's function into waveform inversion for seismic source processes. Geophysical Journal International, **186**: 711–720. doi:10.1111/j.1365-246X.2011.05043.x.

Yagi, Y., Okuwaki, R., Enescu, B., Hirano, S., Yamagami, Y., Endo, S., and Komoro, T. 2014. Rupture process of the 2014 Iquique Chile Earthquake in relation with the foreshock activity. Geophys. Res. Lett., **41**: 4201–4206. doi:10.1002/2014GL060274.

Yagi, Y., Okuwaki, R., Enescu, B., and Lu, J. 2023. Irregular rupture process of the 2022 Taitung, Taiwan, earthquake sequence. Scientific Reports, **13**. Nature Research. doi:10.1038/s41598-023-27384-y.

Yamashita, S., Yagi, Y., and Okuwaki, R. 2022a. Irregular rupture propagation and geometric fault complexities during the 2010 Mw 7.2 El Mayor-Cucapah earthquake. Scientific Reports, **12**: 4575. doi:10.1038/s41598-022-08671-6.

Yamashita, S., Yagi, Y., Okuwaki, R., Shimizu, K., Agata, R., and Fukahata, Y. 2021. Consecutive ruptures on a complex conjugate fault system during the 2018 Gulf of Alaska earthquake. Scientific Reports, **11**: 5979. doi:10.1038/s41598-021-85522-w.

Yamashita, S., Yagi, Y., Okuwaki, R., Shimizu, K., Agata, R., and Fukahata, Y. 2022b. Potency density tensor inversion of complex body waveforms with time-adaptive smoothing constraint. Geophysical Journal International, **231**: 91–107. Oxford University Press (OUP). doi:10.1093/gji/ggac181.

Zhang, H., Koper, K.D., Pankow, K., and Ge, Z. 2017. Imaging the 2016 Mw 7.8 Kaikoura, New Zealand, earthquake with teleseismic P waves: A cascading rupture across multiple faults. Geophysical Research Letters, **44**: 4790–4798. doi:10.1002/2017GL073461.

Zheng, A., Wang, M., Yu, X., and Zhang, W. 2018. Source rupture process of the 2016 Kaikoura, New Zealand earthquake estimated from the kinematic waveform inversion of strong-motion data. Geophysical Journal International, **212**: 1736–1746. doi:10.1093/gji/ggx505.

Figure legends

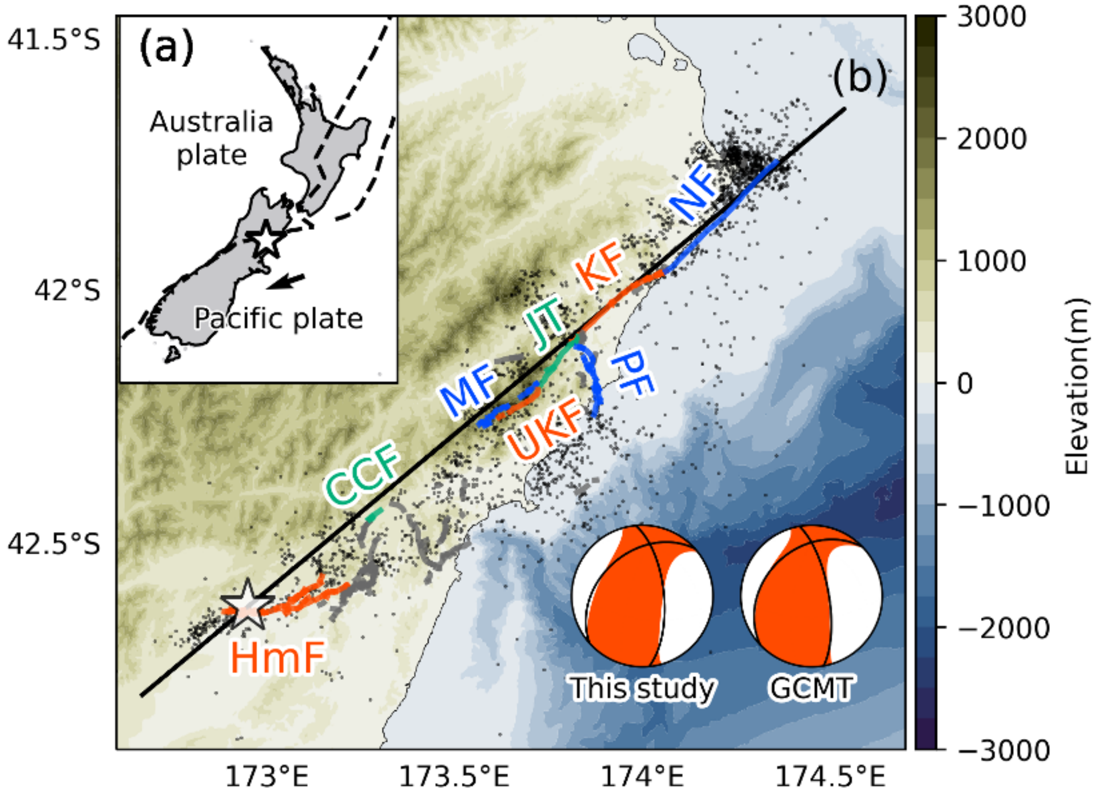

Figure 1. **a** Tectonic setting of the study region. The dashed lines represent the plate boundary (Bird 2003). The arrow denotes the plate motion of the Pacific plate relative to the fixed Australia plate in NUVEL 1A (DeMets et al. 1994). The star marks the mainshock epicenter (Lanza et al. 2019). **b** Seismotectonic summary of the study region of the 2016 Kaikoura earthquake. The left and right beachball show the obtained total moment tensor and the Global Centroid Moment Tensor (Dziewonski et al. 1981, Ekström et al. 2012) solution for the

mainshock, respectively. Black dots represent aftershocks during the week after the mainshock (Lanza et al. 2019). Grey, orange, blue, and green lines indicate surface ruptures of the 2016 Kaikoura earthquake from the New Zealand Active Faults Database (Langridge et al. 2016). The black line represents the assumed model plane. Background contours display topography/bathymetry (Mitchell et al. 2012). HmF–Humps fault zone, CCF–Conway-Charwell fault, MF–Manakau fault, UKF–Upper Kowhai fault, JT–Jordan Thrust, PF–Papatea fault, KF–Kekerengu fault, NF–Needles fault.

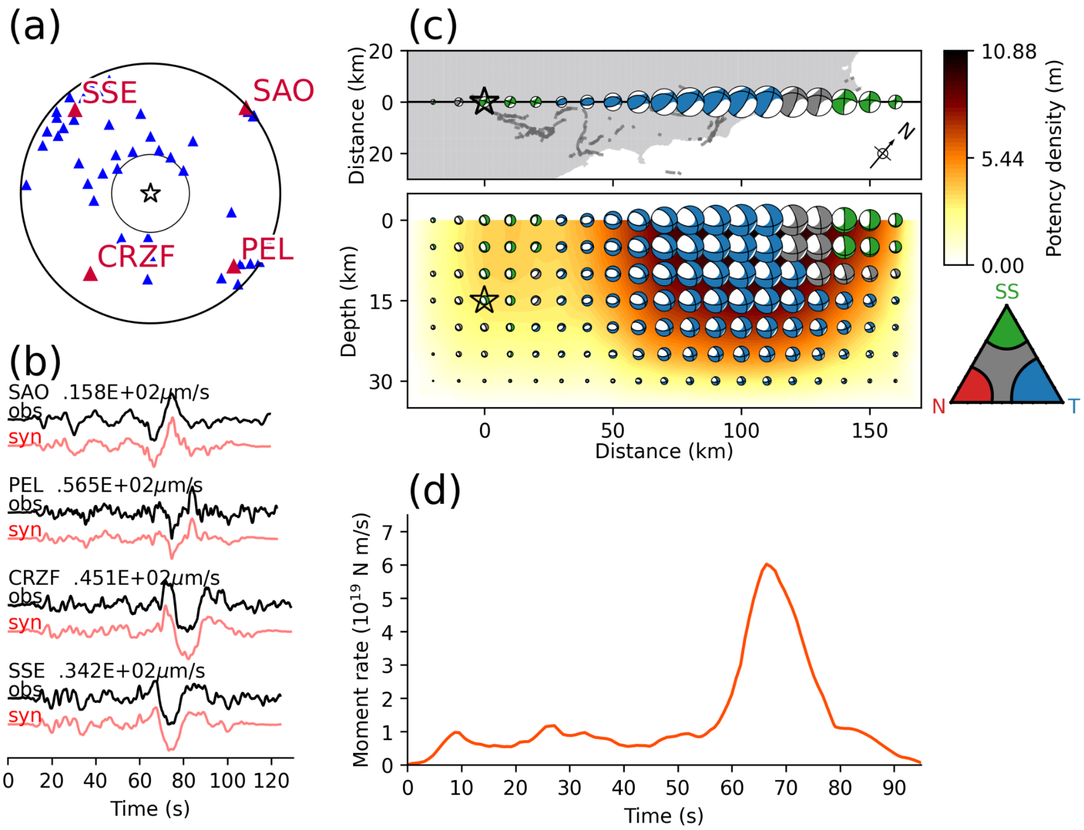

Figure 2. Summary of inversion results. **a** Azimuthal equidistant projection of the station distribution used in the inversion. The star denotes the epicenter (Lanza et al. 2019). Triangles denote station locations; the waveforms for the four stations indicated with red triangles are shown in **b**. The circles represent epicentral distances of 30° and 100°. **b** Observed (upper black trace) and synthetic (lower red trace) waveforms at the stations marked in red in **a**. Station codes and maximum amplitudes are shown at the top. **c** Potency density tensors on the assumed model plane. The map view in the top panel shows the top row of tensors on the assumed model plane, represented by the black line, and grey lines indicate surface ruptures (Langridge et al.

2016). The profile in the bottom panel shows the tensors on the assumed model plane. Note that the beachballs in the map are shown as a lower-hemisphere projection in the map and as a cross-section view from the southeast side in the bottom panel. Beachballs in the bottom panel are colored based on a Frohlich diagram (Frohlich 2001), in which blue is reverse faulting (T), green is strike-slip faulting (SS), red is normal faulting (N), and grey is other. The star denotes the hypocenter (Lanza et al. 2019). **d** Moment-rate function.

641

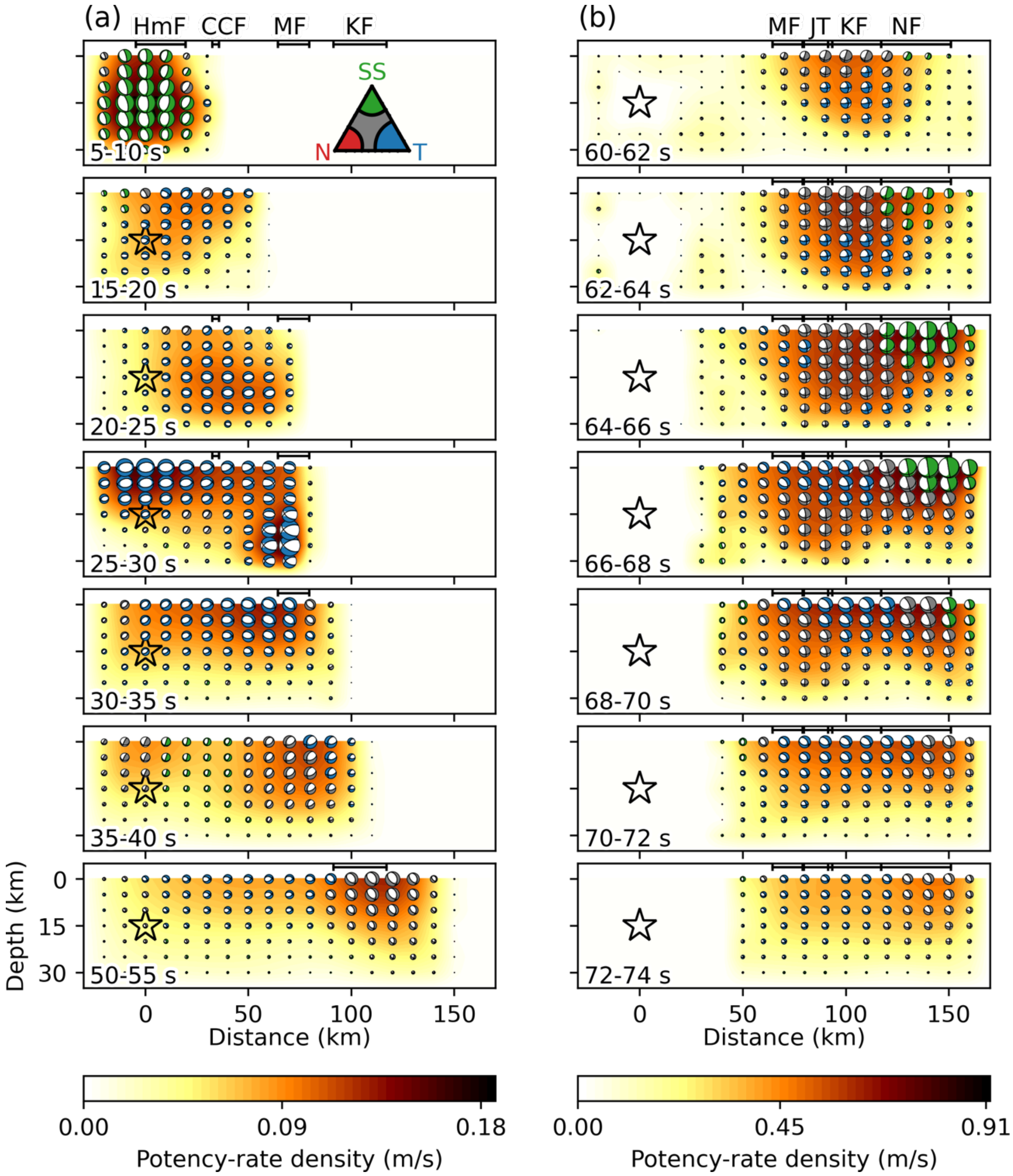

642 Figure 3. Selected snapshots of potency-rate density tensors **a** before 55 s and **b** after 60 s.
643 Beachballs are shown in cross-section view from the southeast side of the assumed model
644 plane. The background color is scaled with the maximum potency-rate density during 0–55 s
645 for **a** and 60–74 s for **b**; note that the scales differ for the two plots. The star denotes the

hypocenter (Lanza et al. 2019). Black bars are the locations of the surface faults (Langridge et al. 2016) projected onto the model plane.

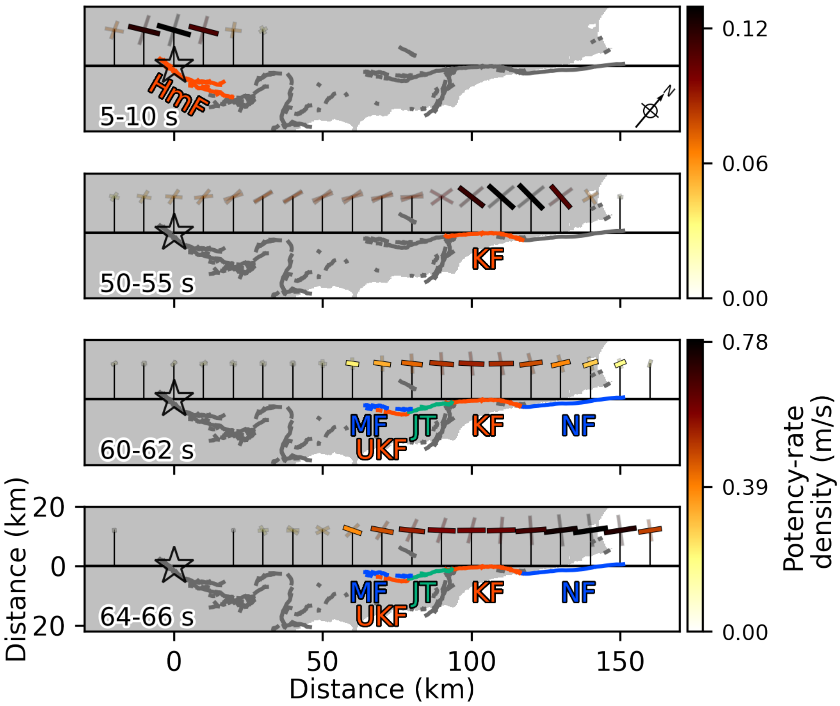

Figure 4. Map views showing selected snapshots of strikes of the potency-rate density tensors (cross marks) in the top row of the model plane. Right-lateral or northwest-dipping nodal planes of tensors with relatively large potency-rate density are emphasized. Note that the color scale changes after 55 s.

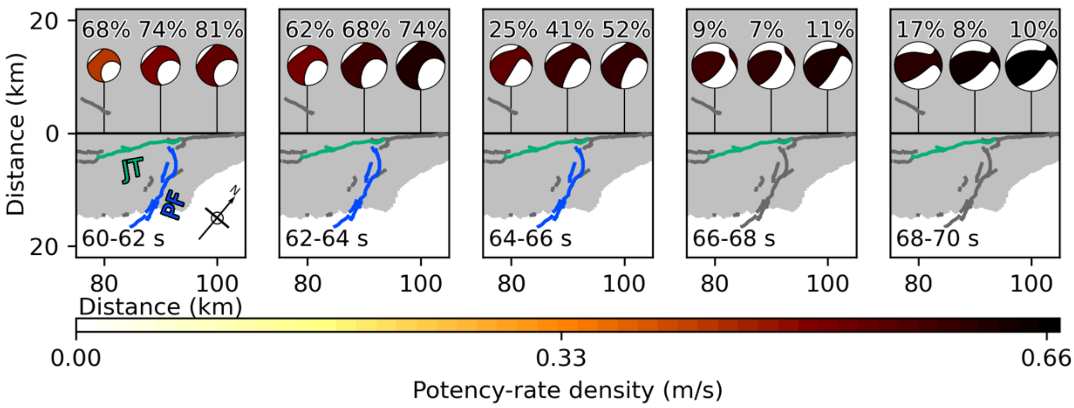

Figure 5. Map views showing selected snapshots of potency-rate density tensors (lower hemisphere projections) between 60 and 70 s in the top row of the model plane 80–100 km northeast of the epicenter. The color of the beachball symbols represents the potency-rate density. Above each symbol is shown the ratio of the non-double-couple component.

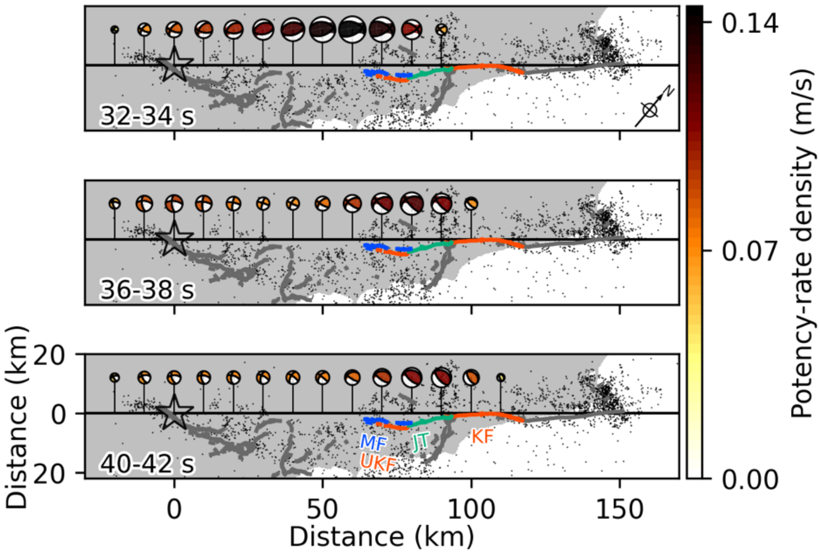

Figure 6. Map views showing selected snapshots of potency-rate density tensors (lower hemisphere projections) between 32 and 42 s in the top row of the entire model plane. Black dots represent aftershocks during the week after the mainshock (Lanza et al. 2019). Grey, orange, blue, and green lines indicate surface faults (Langridge et al. 2016).